Screening effects on the optical properties of II-VI wurtzite ZnO/MgO quantum dots

Seoung-Hwan Park*
Department of Electronics Engineering, Catholic University of Daegu, Hayang, Kyeongsan, Kyeongbuk, 38430 Republic of Korea

Doyeol Ahn
Department of Electrical and Computer Engineering, University of Seoul, 90 Jeonnong, Tongdaimoon-Gu, Seoul, 130-743 Republic of Korea and Physics Department, Charles E Schmidt College of Science, Florida Atlantic University, Boca Raton, Florida 33431-0991, USA

(Received 6 November 2017; revised manuscript received 17 January 2018; published 1 February 2018)

The screening effects on the light emission characteristics of wurtzite (WZ) ZnO/MgZnO quantum dots (QDs) were investigated as a function of carrier density. These results were compared with those without the screening effect. The light emission intensity is shown to be significantly affected by the screening effect. The difference of the light intensity between cases with and without screening effect gradually increases with increasing carrier density. This can be explained by the fact that the overlap between the electron and hole wave functions, and therefore the optical matrix element, is enhanced due to the increase in the screening effect with increasing carrier density. Also, the peak wavelength for the self-consistent solution is observed to be blueshifted with increasing carrier density because the optical matrix elements corresponding to transitions from the conduction subband to higher valence subbands become dominant at a higher carrier density. We observe that the screening effect is enhanced rapidly with increasing dot size. In the case of the ZnO/MgO QD grown on MgO substrate, there exist a large potential due to the strain-induced piezoelectric polarization, in addition to the spontaneous polarization. As a result, its light emission intensity is shown to be much smaller than that of ZnO/MgO QD grown on ZnO substrate.

DOI: 10.1103/PhysRevB.97.075301

I. INTRODUCTION

Short-wavelength gallium nitrite (GaN) quantum dots (QDs) have recently attracted much attention as promising nanostructures for optoelectronic, electronic, and spintronic applications [1–4]. On the other hand, ZnO and related oxides have also been proposed as other wide band-gap semiconductors for short-wavelength optoelectronic applications because they have several advantages over III-V nitrides [5–7]. Experimental results showed that ZnO quantum dots (QDs) are promising for device applications and their photoluminescence quantum efficiency is much higher than their bulk counterparts [8–11].

Recently, several groups theoretically investigated electronic and optical properties such as the exciton binding energies, the optical gain, and interband optical transition of wurtzite (WZ) ZnO QDs, ZnO/MgZnO QDs, and coupled QDs [12–15]. These results showed the optical and electronic properties of the QDs can be affected by several structural parameters such as dot height and the barrier thickness. In particular, we expect that the optical properties will be significantly affected by the built-in electric field due to piezoelectric (PZ) and spontaneous (SP) polarizations [16,17]. However, there has been very little work done on screening effects by injected carriers on optical properties of WZ ZnO/MgO QD structures with the built-in electric field. This will be very important as a design guide for optoelectronic device applications such as laser diodes (LDs) and light-emitting diodes (LEDs) related to ZnO-based QD structures.

In this paper we investigate screening effects on light emission characteristics for WZ ZnO/MgO quantum dots with PZ and SP polarizations using an effective mass theory. ZnO/MgO quantum dots are commonly synthesized in a wet-chemical process and exhibit spherical or core-shell shape [18,19]. Real quantum dot is well approximated by a simplified quantum dot structure of the same volume and shape [20]. Here we consider a cubic QD structure (ZnO) of a length d, instead of spherical quantum dot with a diameter d, which is embedded in MgO cladding material with a size of $200 \times 200 \times 200$ Å^3. Also, we used a six-band model for the holes as an approximation because the coupling between electrons and holes is relatively weak due to large band gap energy for ZnO [21]. The self-consistent eigenvalues and wave functions are obtained by solving the Schrödinger equation for electrons, the 6×6 Hamiltonian for holes, and Poisson's equation iteratively [22,23].

II. THEORETICAL MODEL

A. Hamiltonians for electrons and holes

The effective-mass Hamiltonian for the conduction band can be written as [23,24]

$$H_c(\mathbf{k},\epsilon) = \frac{\hbar^2}{2m_e}\left(k_x^2 + k_y^2 + k_z^2\right) + E_c^0 + P_{c\epsilon}, \qquad (1)$$

*shpark@cu.ac.kr

where m_e is the electron effective mass. The band edge energy is given by

$$E_c^0 = \Delta_1 + \Delta_2 + E_g + P_{c\epsilon}, \tag{2}$$

which includes a hydrostatic energy shift

$$P_{c\epsilon} = a_c(\epsilon_{xx} + \epsilon_{yy} + \epsilon_{zz}), \tag{3}$$

where a_c is the conduction-band deformation potential, E_g is the band-gap energy, Δ_1 is the crystal-field split energy, $\Delta_i (i = 2,3)$ account for spin-orbit interactions, k_i is the wave vector, and ϵ_{ij} is the strain tensor.

The Hamiltonian for the valence-band structure can be derived by using the $\mathbf{k}\cdot\mathbf{p}$ method and the c-plane Hamiltonian for the (0001)-oriented wurtzite crystal can be written as [22,23]

$$H(\mathbf{k},\epsilon) = -\begin{pmatrix} F & -K^* & -H^* & 0 & 0 & 0 \\ -K & G & H & 0 & 0 & \Delta \\ -H & H^* & \lambda & 0 & \Delta & 0 \\ 0 & 0 & 0 & F & -K & H \\ 0 & 0 & \Delta & -K^* & G & -H^* \\ 0 & \Delta & 0 & H^* & -H & \lambda \end{pmatrix} \begin{matrix} |U_1\rangle \\ |U_2\rangle \\ |U_3\rangle \\ |U_4\rangle \\ |U_5\rangle \\ |U_6\rangle, \end{matrix} \tag{4}$$

where

$$\begin{aligned} F &= \Delta_1 + \Delta_2 + \lambda + \theta, \\ G &= \Delta_1 - \Delta_2 + \lambda + \theta, \\ \lambda &= \frac{\hbar^2}{2m_o}\left[A_1 k_z^2 + A_2\left(k_x^2 + k_y^2\right)\right] + D_1\epsilon_{zz} + D_2(\epsilon_{xx} + \epsilon_{yy}), \\ \theta &= \frac{\hbar^2}{2m_o}\left[A_3 k_z^2 + A_4\left(k_x^2 + k_y^2\right)\right] + D_3\epsilon_{zz} + D_4(\epsilon_{xx} + \epsilon_{yy}), \\ K &= \frac{\hbar^2}{2m_o}A_5(k_x + ik_y)^2, \\ H &= \frac{\hbar^2}{2m_o}A_6(k_x + ik_y)k_z, \\ \Delta &= \sqrt{2}\Delta_3. \end{aligned} \tag{5}$$

Here the A_i's are the valence-band effective-mass parameters and the D_i's are the deformation potentials for wurtzite crystals. The bases for the Hamiltonian are defined as [22]

$$\begin{aligned} |U_1\rangle &= -\frac{1}{\sqrt{2}}|(X + iY)\uparrow\rangle, \\ |U_2\rangle &= \frac{1}{\sqrt{2}}|(X - iY)\uparrow\rangle, \\ |U_3\rangle &= |Z\uparrow\rangle, \\ |U_4\rangle &= \frac{1}{\sqrt{2}}|(X - iY)\downarrow\rangle, \\ |U_5\rangle &= -\frac{1}{\sqrt{2}}|(X + iY)\downarrow\rangle, \\ |U_6\rangle &= |Z\downarrow\rangle. \end{aligned} \tag{6}$$

B. Strain and static electric potential

The strain tensors and built-in potential are obtained by [25]

$$\begin{aligned} \sigma_{ij} &= C_{\text{ijlm}}\epsilon_{ij} - e_{kji}E_k, \\ D_i &= \epsilon_0\epsilon_r E_j + P_i + P_{\text{sp}}, \end{aligned} \tag{7}$$

where σ are vectors of the stress and D is the electric flux, which are related to the strain ϵ and electric field E vectors. Here C_{ijlm}, P_i, ϵ_r, and P_{sp} are the elastic moduli, the piezoelectric polarization, relative dielectric constants, and spontaneous polarization, respectively. The strain-induced piezoelectric polarization P_i is given by [20]

$$P_i = e_{ijk}\epsilon_{jk}, \tag{8}$$

where e_{kji} is the piezoelectric coefficient. The total polarization in the right-hand side of Eq. (7) is given by [20]

$$\mathbf{P} = \begin{pmatrix} 2e_{15}\epsilon_{13} \\ 2e_{15}\epsilon_{23} \\ e_{31}(\epsilon_{11} + \epsilon_{22}) + e_{33}\epsilon_{33} + P_{\text{sp}} \end{pmatrix}. \tag{9}$$

The elastic strain and built-in potential were calculated by using COMSOL Multiphysics based on the theory of continuum elasticity [26]. The QD is initially strained by ϵ_0 in all three directions. The misfit strain ϵ_0 of the QD is taken with respect to the surrounding matrix and is assumed to be equal to $(2\epsilon_{0a} + \epsilon_{0c})/3$, where ϵ_{0a} is the misfit strain in the x-y plane and ϵ_{0c} is the misfit strain along the z plane [20].

C. Self-consistent calculation

The total potential profiles for the electrons and holes are [27]

$$\begin{aligned} V_c(\mathbf{r}) &= V_{cb}(\mathbf{r}) + V(\mathbf{r}) - |e|\phi(\mathbf{r}), \\ V_v(\mathbf{r}) &= V_{vb}(\mathbf{r}) - V(\mathbf{r}) + |e|\phi(\mathbf{r}), \end{aligned} \tag{10}$$

where V_{cb} and V_{vb} are the square potential for the conduction band and valence band, respectively, V is the static electric potential induced by the piezoelectric and spontaneous polarizations, and ϕ is the screening potential induced by the charged carriers, which satisfies Poisson's equation

$$\nabla\cdot[\epsilon(\mathbf{r})\nabla\phi(\mathbf{r})] = -|e|[p(\mathbf{r}) - n(\mathbf{r})], \tag{11}$$

where ϵ is the dielectric constant. The density of state for a quantum dot is given by $\rho(E) = \delta(E - E_{n,m})/V$, where V is the volume of the QD. Then, the quasi-Fermi levels for a given carrier density are calculated from the charge neutrality using

the following relations [25]:

$$n = \frac{2}{V}\sum_{n}\frac{1}{1+\exp\left[\frac{(E_n - E_{fc})}{kT}\right]},$$
$$p = \frac{1}{V}\sum_{m}\frac{1}{1+\exp\left[\frac{(E_m - E_{fv})}{kT}\right]}, \quad (12)$$

where E_{fc} and E_{fv} are the relevant quasi-Fermi levels. Here we assumed that carriers are injected into the QD and the contribution from continuum states is negligible in Eq. (12). The electron and hole concentrations $p(\mathbf{r})$ and $n(\mathbf{r})$ in Eq. (11) are related to the wave functions of the nth conduction subband and the mth valence subband by [25]

$$n(\mathbf{r}) = 2\sum_{n}|\phi_n(\mathbf{r})|^2\frac{1}{1+\exp\left[\frac{(E_n - E_{fc})}{kT}\right]} \quad (13)$$

and

$$p(\mathbf{r}) = \sum_{m}\sum_{\nu=1}^{6}|g_m^{(\nu)}(\mathbf{r})|^2\frac{1}{1+\exp\left[\frac{(E_m - E_{fv})}{kT}\right]}, \quad (14)$$

where ν refers to the bases for the Hamiltonian, and $\phi_n(\mathbf{r})$ and $g_m^{(\nu)}(\mathbf{r})$ ($\nu = 1,2,3,4,5$, and 6) are envelope functions in the conduction and valence bands, respectively.

D. Optical matrix element and spontaneous emission coefficient

The optical momentum matrix elements $\mathbf{M}$ for the QD are given by [23]

$$|\hat{\mathbf{e}}\cdot\mathbf{M}|^2 = \left|\left\langle\Psi_c^n\middle|\hat{\mathbf{e}}\cdot\mathbf{p}\middle|\Psi_h^m\right\rangle\right|^2, \quad (15)$$

where Ψ_c and Ψ_h are the wave functions for the conduction and the valence bands, respectively. The indices $n = \{n_1 n_2 n_3\}$ and $m = \{m_1 m_2 m_3\}$ denote the electron states in the conduction band and the subband states in the valence band, respectively. The polarization-dependent interband momentum-matrix elements can be written as [24]

TE polarization ($\hat{\mathbf{e}} = \cos\phi\hat{\mathbf{x}} + \sin\phi\hat{\mathbf{y}}$) :

$$|\hat{\mathbf{e}}\cdot\mathbf{M}^{\uparrow}|^2 = \left|\cos\phi\left\{-\frac{1}{\sqrt{2}}P_x\langle g_m^{(1)}|\phi_n\rangle + \frac{1}{\sqrt{2}}P_x\langle g_m^{(2)}|\phi_n\rangle\right\}\right.$$
$$\left. + \sin\phi\left\{-i\frac{1}{\sqrt{2}}P_x\langle g_m^{(1)}|\phi_n\rangle - i\frac{1}{\sqrt{2}}P_x\langle g_m^{(2)}|\phi_n\rangle\right\}\right|^2, \quad (16)$$

$$|\hat{\mathbf{e}}\cdot\mathbf{M}^{\downarrow}|^2 = \left|\cos\phi\left\{\frac{1}{\sqrt{2}}P_x\langle g_m^{(4)}|\phi_n\rangle - \frac{1}{\sqrt{2}}P_x\langle g_m^{(5)}|\phi_n\rangle|\phi_n\rangle\right\}\right.$$
$$\left. + \sin\phi\left\{-i\frac{1}{\sqrt{2}}P_x\langle g_m^{(4)}|\phi_n\rangle - i\frac{1}{\sqrt{2}}P_x\langle g_m^{(5)}|\phi_n\rangle\right\}\right|^2, \quad (17)$$

TM polarization ($\hat{\mathbf{e}} = \hat{\mathbf{z}}$):

$$|\hat{\mathbf{e}}\cdot\mathbf{M}^{\uparrow}|^2 = \left|P_z\langle g_m^{(3)}|\phi_n\rangle\right|^2, \quad (18)$$

$$|\hat{\mathbf{e}}\cdot\mathbf{M}^{\downarrow}|^2 = \left|P_z\langle g_m^{(3)}|\phi_n\rangle\right|^2. \quad (19)$$

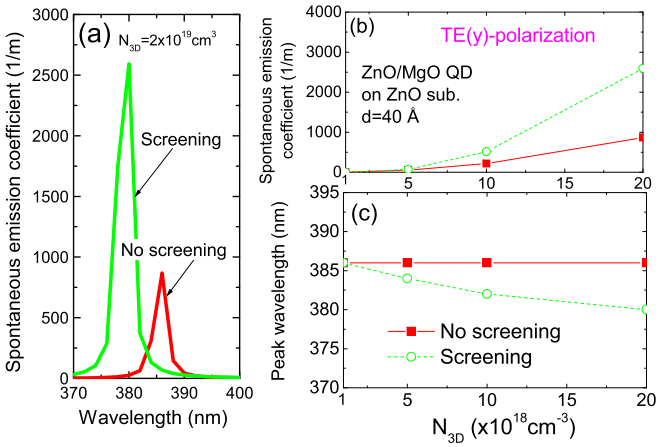

FIG. 1. (a) TE(y)-polarized spontaneous emission spectra, (b) peak intensity, and (c) peak wavelength as a function of a carrier density for wurtzite ZnO/MgO QDs grown on ZnO substrate without and with the screening effect. The length d of cubic QD is set to be 40 Å. The self-consistent results for the spontaneous emission spectra were calculated at the carrier density of $N_{3d} = 2\times10^{19}$ cm^{-3}.

Also,

$$P_x = P_y = \langle S|p_x|X\rangle = \langle S|p_y|Y\rangle$$
$$= \frac{m_o}{\hbar}P_2, P_z = \langle S|p_z|Z\rangle = \frac{m_o}{\hbar}P_1,$$
$$P_1^2 = \frac{\hbar^2}{2m_o}\left(\frac{m_o}{m_e^z} - 1\right)\frac{(E_g + \Delta_1 + \Delta_2)(E_g + 2\Delta_2) - 2\Delta_3^2}{E_g + 2\Delta_2},$$
$$P_2^2 = \frac{\hbar^2}{2m_o}\left(\frac{m_o}{m_e^t} - 1\right)$$
$$\times\frac{E_g\left[(E_g + \Delta_1 + \Delta_2)(E_g + 2\Delta_2) - 2\Delta_3^2\right]}{(E_g + \Delta_1 + \Delta_2)(E_g + \Delta_2) - \Delta_3^2}. \quad (20)$$

The spontaneous emission coefficient for the quantum dot is [17]

$$g_{\rm sp}(\hbar\omega) = \frac{e^2}{m_o^2\omega}\sqrt{\frac{\mu_o}{\epsilon}}\sum_{n,m}\frac{1}{V}\left|\hat{\mathbf{e}}\cdot\mathbf{M}_m^n\right|^2$$
$$\times\frac{\hbar/\tau_{\rm in}}{\left(E_{hm}^{en} - \hbar\omega\right)^2 + (\hbar/\tau_{\rm in})^2}\left(f_c^n - f_v^m\right), \quad (21)$$

where m_o is the free-electron mass, ω is the angular frequency, μ_o is the vacuum permeability, and $\tau_{\rm in}$ is the intraband relaxation time, which is assumed to be 1×10^{-13} s. The material parameters for ZnO and MgO used in the *computations* were taken from Ref. [28]. Also, we used values of -0.034 and -0.135 C/m^2 for spontaneous polarizations of ZnO and MgO [29].

III. RESULTS AND DISCUSSION

Figure 1 shows (a) TE(y)-polarized spontaneous emission spectra, (b) peak intensity, and (c) peak wavelength as a function of a carrier density for wurtzite ZnO/MgO QDs grown on ZnO substrate without and with the screening effect. The length d of cubic QD is set to be 40 Å. The self-consistent results for the spontaneous emission spectra

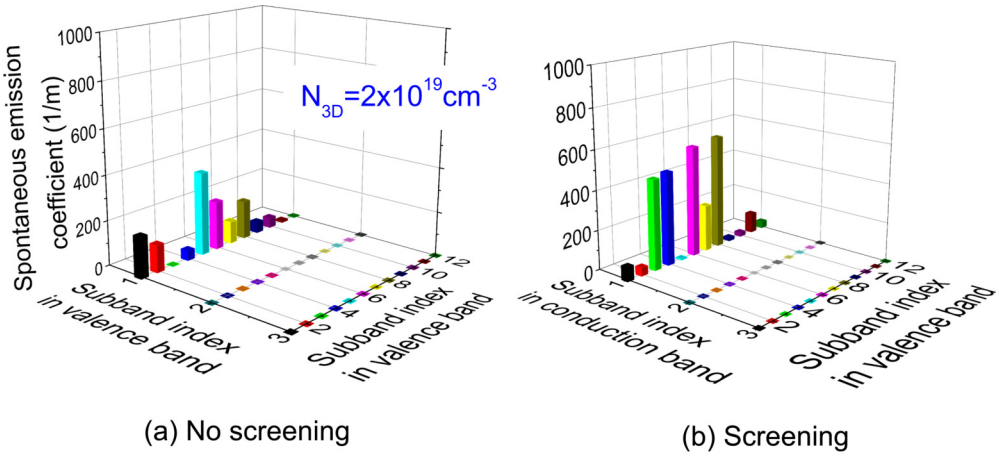

FIG. 2. Peak spontaneous emission coefficient for each subband transition of wurtzite ZnO/MgO QDs grown on ZnO substrate without and with the screening effect.

were calculated at the carrier density of $N_{3d} = 2 \times 10^{19}$ cm^{-3}. We observe that the light emission intensity is significantly affected by the screening effect. The spontaneous emission coefficient at $N_{3d} = 2 \times 10^{19}$ cm^{-3} is about three times larger than that without considering screening effect. Also, the peak wavelength for the self-consistent solution is shown to be blueshifted, compared to that without the screening effect, and the peak wavelength difference between two cases gradually increases with increasing carrier density. This can be explained by the fact that, in the case of the self-consistent solution, the optical matrix element corresponding to transitions from the first conduction subband to higher valence subbands becomes dominant at a higher carrier density, as discussed below.

Figure 2 shows a peak spontaneous emission coefficient for each subband transition of wurtzite ZnO/MgO QDs grown on ZnO substrate without and with the screening effect. The self-consistent results were calculated at the carrier density of $N_{3d} = 2 \times 10^{19}$ cm^{-3}. The x or y coordinate indicates the subband index in the conduction or valence band. For example, $(x, y) = (1,4)$ means the peak spontaneous emission coefficient corresponding to the transition between the first subband in the conduction band and the fourth subband in the valence band. We observe that the emission intensity is dominated by the transition related to the first subband in the conduction band. The light intensity by the transition from the second or higher subbands in the conduction band is negligible. Also, the peak spontaneous emission coefficients with the screening effect are much larger than those without the screening effect. In the case without band-mixing effect, the first six subbands in the valence band are degenerate. However, these subband energies are splitted with the inclusion of the band-mixing effect, which will affect spatial distribution of wave function.

Figure 3 shows a normalized optical matrix element for TE polarization of wurtzite ZnO/MgO QDs grown on ZnO substrate without and with the screening effect. The self-consistent results were calculated at the carrier density of $N_{3d} = 2 \times 10^{19}$ cm^{-3}. The x or y coordinate indicates the subband index in the conduction or valence band. In the case without screening, we observe that the matrix elements corresponding to the transition between the second or third subband in the conduction band and subbands in the valence band are dominant. However, the light intensity by the transition between the second or third subband in the conduction

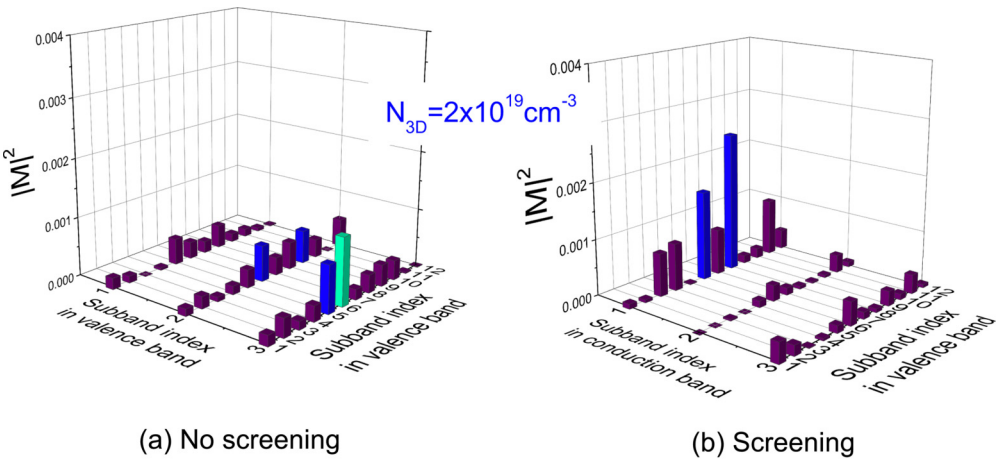

FIG. 3. Normalized optical matrix element for TE polarization of wurtzite ZnO/MgO QDs grown on ZnO substrate without and with the screening effect.

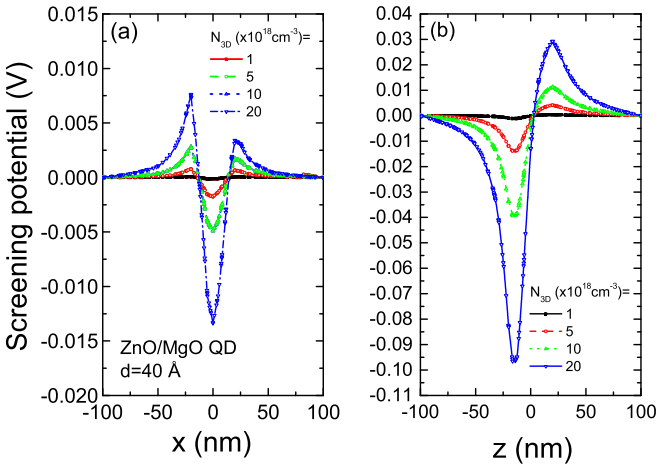

FIG. 4. Screening potential $\phi(\mathbf{r})$ along x and z axes for wurtzite ZnO/MgO QDs.

band and subbands in the valence band is relatively low, as shown in Fig. 2. This can be explained by the fact that the electron population in higher subbands is relatively low. On the other hand, in the case of the self-consistent case, the matrix element corresponding to the transition between the first subband in the conduction band and subbands in the valence band is shown to be dominant. Simultaneously, the matrix elements with the screening effect are much larger than those without the screening effect. Hence, the peak wavelength for the self-consistent solution is shorter than that without the screening effect because the transition energy of the former is larger than that of the latter.

Figure 4 shows the screening potential $\phi(\mathbf{r})$ along x and z axes for wurtzite ZnO/MgO QDs grown on ZnO substrate.

We observe that the screening potential rapidly increases with increasing carrier density. Also, the screening effect along the z axis is larger than that along the x axis because there exists the internal field along the z axis. The increase in the screening potential will affect the optical matrix elements. For example, the matrix element between the first subband in the conduction band and the third subband in the valence band is greatly enhanced by the screening effect, as shown in Fig. 3 . Its value was mainly determined by the matrix element $|\hat{\mathbf{e}} \cdot \mathbf{M}^{\downarrow}|^2$ of the lower block. Thus, we can analyze these results by calculating overlap integrals in $|\hat{\mathbf{e}} \cdot \mathbf{M}^{\downarrow}|^2$.

Figure 5 shows the overlap integral for $\langle g_m^{(4)}|\phi_1\rangle$ and $\langle g_m^{(5)}|\phi_1\rangle$ $(m = 3)$ as a function of the carrier density. In Eq. (17) we see that the y-polarized matrix element is given by the difference between overlap integrals $\langle g_m^{(4)}|\phi_1\rangle$ and $\langle g_m^{(5)}|\phi_1\rangle$. The overlap integral for $\langle g_m^{(4)}|\phi_n\rangle$ is shown to be nearly independent of the carrier density while that for $\langle g_m^{(5)}|\phi_n\rangle$ gradually decreases and shows sign change at the carrier density of $N_{3d} = 1.2 \times 10^{19}$ cm^{-3}. Thus, the matrix element is enhanced because two overlap integrals have the same sign. On the other hand, in the case without screening effect, the absolute values of $\langle g_3^{(4)}|\phi_1\rangle$ and $\langle g_3^{(5)}|\phi_1\rangle$ are similar to each other and thus the matrix element becomes very small. The increase in optical matrix elements for the other transitions could be also explained by similar analysis. As a result, we know that the consideration of the screening effect is very

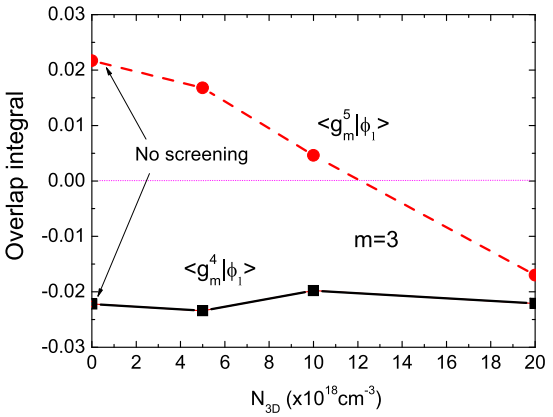

FIG. 5. Overlap integral for $\langle g_m^{(4)}|\phi_1\rangle$ and $\langle g_m^{(5)}|\phi_1\rangle$ $(m = 3)$ as a function of the carrier density.

important in predicting optical properties of WZ ZnO-based QD devices.

Figure 6 shows (a) potential due to piezoelectric and spontaneous polarizations along the z axis, (b) screening potential along the z axis, and (c) spontaneous emission spectra for wurtzite ZnO/MgO QDs grown on GaN substrate with several dot size ($d = 20$, 40, and 60 Å). The potential along the z axis increases with increasing dot size because it is given by the product of the dot size and the internal field. Also, the screening potential is enhanced rapidly with increasing dot size. In the case of relatively small dot size ($d = 20$ Å), the screening effect is shown to be negligible. Thus, the peak wavelength is not nearly affected by the screening effect and the peak intensity with the screening effect is rather smaller than that without the screening effect. On the other hand, in the case of a large dot size ($d = 60$ Å), the blueshift of the peak wavelength is greatly increased due to a large screening potential. However, the increasing rate in the light intensity due the screening effect is smaller than that for the case with smaller dot size ($d = 40$ Å). This is mainly attributed to the fact

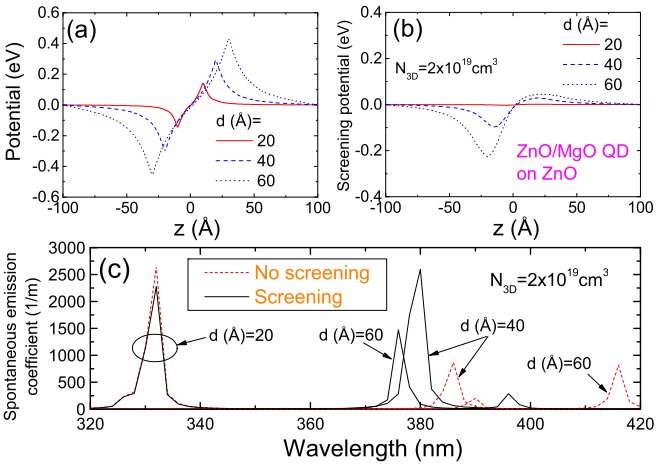

FIG. 6. (a) Potential due to piezoelectric and spontaneous polarizations along the z axis, (b) screening potential along the z axis, and (c) spontaneous emission spectra for wurtzite ZnO/MgO QDs grown on GaN substrate with several dot size ($d = 20$, 40, and 60 Å).

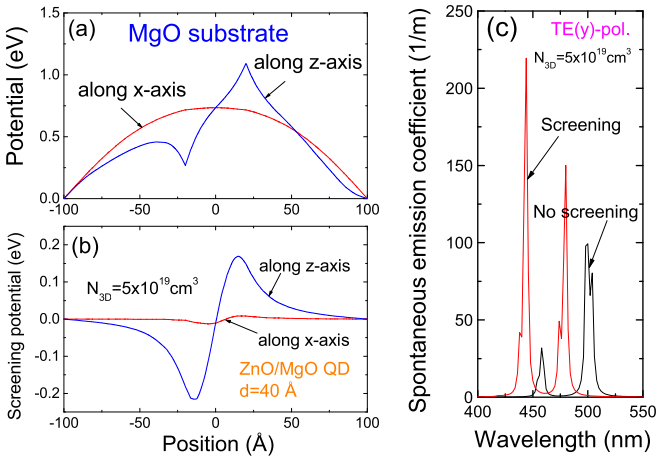

FIG. 7. (a) Potential due to piezoelectric and spontaneous polarizations along x and z axes, (b) screening potential along x and z axes, and (c) spontaneous emission spectra for wurtzite ZnO/MgO QDs grown on MgO substrate ($d = 40$ Å).

that the quasi-Fermi level is decreased with the inclusion of the screening potential due to the reduction in carrier confinement in potential well.

Figure 7 shows (a) potential due to piezoelectric and spontaneous polarizations along x and z axes, (b) screening potential along x and z axes, and (c) spontaneous emission spectra for wurtzite ZnO/MgO QDs grown on MgO substrate ($d = 40$ Å). The self-consistent results were calculated at the carrier density of $N_{3d} = 5 \times 10^{19}$ cm^{-3}. The ZnO/MgO QD grown on MgO substrate shows that there exists a large potential due to the strain-induced piezoelectric polarization, in addition to the spontaneous polarization. That is, there exists the large potential along the x axis. As a result, the light emission intensity is observed to be much smaller than that of ZnO/MgO QD grown on ZnO substrate. Also, the light intensity is greatly enhanced by the screening effect because of a larger screening potential along the z axis, similarly to that observed for QD structure grown on ZnO substrate. On the other hand, we observe that the screening potential along the z axis is much smaller than that along the z axis, despite the potential magnitude of the former being comparable to that of the latter. This may be explained by the fact that the carrier confinement is enhanced due to a triangular conduction (valence) band shape along the z axis.

IV. SUMMARY

In summary, the screening effects on light emission characteristics of WZ ZnO/MgO QDs were investigated as a function of carrier density. These results were compared with those without the screening effect. The light emission characteristics are shown to be significantly affected by the screening effect. The difference of the light intensity between cases with and without screening effect increases with increasing carrier density. This can be explained by the fact that the optical matrix elements are enhanced due to the screening effect with increasing carrier density. The peak wavelength for the self-consistent solution is blueshifted with increasing carrier density because the optical matrix elements related to transitions to higher valence subbands become dominant at higher carrier density. We observe that the screening effect is enhanced rapidly with increasing dot size and, as a result, the blueshift of the peak wavelength is greatly increased with increasing dot size. In the case of the ZnO/MgO QD grown on MgO substrate, its light emission intensity is observed to be much smaller than that of ZnO/MgO QD grown on ZnO substrate.

ACKNOWLEDGMENTS

This research was supported by Basic Science Research Program through the National Research Foundation of Korea (NRF) funded by the Ministry of Education, Science and Technology (2015R1D1A1A01057110).

[1] S. C. Davies, D. J. Mowbray, F. Ranalli, and T. Wang, Appl. Phys. Lett. **96**, 251904 (2010).
[2] S. Schulz and E. P. O'Reilly, Phys. Status Solidi B **249**, 516 (2012).
[3] X. Yang, M. Arita, S. Kako, and Y. Arakawa, Phys. Status Solidi C **9**, 613 (2012).
[4] S.-H. Park and D. Ahn, J. Appl. Phys. **112**, 043107 (2012).
[5] B. P. Zhang, N. T. Binh, K. Wakatsuki, C. Y. Liu, Y. Segawa, and N. Usami, Appl. Phys. Lett. **86**, 032105 (2005).
[6] T. Makino, C. H. Chia, N. T. Tuan, H. D. Sun, Y. Segawa, M. Kawasaki, A. Ohtomo, K. Tamura, and H. Koinuma, Appl. Phys. Lett. **77**, 975 (2000).
[7] N. S. Minimala, A. J. Peter, and C. K. Yoo, J. Comput. Theor. Nanosci. **11**, 257 (2014).
[8] F. Wang, D. Zhao, Z. Guo, L. Liu, Z. Zhang, and D. Shen, Nanoscale **5**, 2864 (2013).
[9] Q. Qiao, B. H. Li, C. X. Shan, J. S. Liu, J. Yu, X. H. Xie, Z. Z. Zhang, T. B. Ji, Y. Jia, and D. Z. Shen, Mater. Lett. **74**, 104 (2012).
[10] J. J. Huang, Y. B. Ye, Z. Q. Lei, X. J. Ye, M. Z. Rong, and M. Q. Zhang, Phys. Chem. Chem. Phys. **16**, 5480 (2014).
[11] B. Efafi, M. S. Ghamsari, M. A. Aberoumand, M. H. Majles Ara, A. H. S. Ghamsari, and H. H. Rad, Phys. Status Solidi A **211**, 2426 (2014).
[12] V. A. Fonoberov and A. A. Balandin, J. Nanoelectron. Optoelectron. **1**, 19 (2006).
[13] M. A. Al-Mossawi, A. H. Al-Khursan, and R. A. Al-Ansari, Recent Pat. Electr. Eng. **2**, 226 (2009).
[14] X. Zhao, S. Y. Wei, and C. X. Xia, Superlattices Microstruct. **50**, 207 (2011).
[15] Z. Zeng, C. S. Garoufalis, S. Baskoutas, and G. Bester, Phys. Rev. B **87**, 125302 (2013).
[16] G. L. Su, T. Frost, P. Bhattacharya, J. M. Dallesasse, and S. L. Chuang, Opt. Express **22**, 22716 (2014).
[17] D. Bimberg, M. Grundmann, and N. N. Ledentsov, *Quantum Dot Heterostructure* (Wiley, New York, 1999).
[18] V. A. Fonoberov and A. A. Balandin, J. Phys.: Condens. Matter **17**, 1085 (2005).

[19] D. Bera, L. Qian, and P. H. Holloway, J. Phys. D: Appl. Phys. **41**, 182002 (2008).
[20] D. P. Williams, A. D. Andreev, E. P. O'Reilly, and D. A. Faux, Phys. Rev. B **72**, 235318 (2005).
[21] A. D. Andreev and E. P. O'Reilly, MRS Int J. Nitr. Sem. **Res4S1**, G6.45 (1999).
[22] S. L. Chuang, IEEE J. Quantum Electron. **32**, 1791 (1996).
[23] S. H. Park and S. L. Chuang, Phys. Rev. B **59**, 4725 (1999).
[24] D. Ahn and S.-H. Park, *Engineering Quantum Mechanics* (Wiley-IEEE, Singapore, 2011), Chap. 3.
[25] F. Boxberg and J. Tulkki, Rep. Prog. Phys. **70**, 1425 (2007).
[26] For example, see http://www.comsol.com/.
[27] S. H. Park and S. L. Chuang, Appl. Phys. Lett. **72**, 3103 (1998).
[28] S.-H. Park and D. Ahn, Opt. Quantum Electron. **38**, 935 (2006).
[29] K. Shimada, N. Takahashi, Y. Nakagawa, T. Hiramatsu, and H. Kato, Phys. Rev. B **88**, 075203 (2013).